Improved Waveform Fidelity Using Local HYPR Reconstruction (HYPR LR)

Kevin M. Johnson,[1*] Julia Velikina,[1] Yijing Wu,[1] Steve Kecskemeti,[1,2] Oliver Wieben,[1,3] and Charles A. Mistretta[1,3]

The recently introduced HYPR (HighlY constrained backPRojection) method allows reconstruction of serial images from highly undersampled data. In HYPR, individual timeframes are obtained via unfiltered backprojections of normalized sinograms using anatomical constraints provided by a composite image. Here we develop the idea of constraining the backprojected data further to a series of local regions of interest in order to decrease the corruption of local information by distant signals. HYPR LR (local reconstruction) permits the use of a longer temporal window in the formation of the composite image, resulting in increased signal-to-noise ratio and quantitative reconstruction accuracy. Unlike HYPR, the new HYPR LR method can be applied to images acquired with arbitrary *k*-space trajectories. It is suitable for a broad range of medical imaging applications involving serial changes in image sequence, offering exciting new opportunities in the future. Magn Reson Med 59:456–462, 2008. © 2008 Wiley-Liss, Inc.

Key words: HYPR; local reconstruction; waveform fidelity

Dynamic MR imaging applications often require compromises in spatial and/or temporal resolution when standard reconstruction schemes are used. Acquisition windows are limited by the passage of contrast agents, as with hyperpolarized nuclei and contrast enhanced angiography, and/or clinical feasibility, as in 3D cine flow imaging. Recently, several alternative sampling and reconstruction methods have been introduced that explore data redundancies in such applications. These methods include model-based reconstructions (1–3) that rely on a priori information and compressed sensing methods (4,5), which aim to reduce the number of *k*-space points to represent a given object.

Recently, HighlY constrained backPRojection (HYPR) (3) reconstruction has been used in conjunction with undersampled radial acquisitions to permit radial undersampling factors of up to 80 in 2D and 1000 in 3D (6–8) in selected time-resolved applications in which the images are sparse and have a high degree of spatiotemporal correlation. Unlike other acceleration methods, where signal-to-noise ratio (SNR) tends to decrease in proportion to the square root of the acceleration factor, HYPR maintains SNR from the composite image used to constrain the unfiltered backprojection process. While originally formulated for angiography, HYPR has been applied to a wide range of imaging methods including hyperpolarized gas imaging, cerebral diffusion, and cine phase contrast, all of which have temporal information that is spatially correlated.

In the original HYPR method, a series of radial acquisitions with interleaved *k*-space projection sets is acquired. Using 1D discrete Fourier transform, we obtain image space profiles P_i^i, $i = 1 \ldots N_p$, where N_p is the number of projections acquired at each timeframe. Each of these Radon projections is then normalized by the corresponding Radon projections P_c^i, $i = 1 \ldots N_p$, of the composite image I_c that is reconstructed by conventional methods from the projections in several or all of the acquired timeframes. An unfiltered backprojection operator B is applied to each normalized projection. The average of all the backprojected information for each timeframe may be regarded as a weighting image I_w. The individual timeframe weighting images provide dynamic information. The final HYPR images I_H are obtained by multiplication of the individual timeframe weighting images with the composite image, and can be described as:

$$I_H(t) = I_c \cdot I_w(t) = I_c \cdot \frac{1}{N_p} \sum_{i=1}^{N_p} B\left(\frac{P_t^i}{P_c^i}\right) \quad [1]$$

In the limit of extremely sparse images or images with complete spatiotemporal correlation the HYPR algorithm provides near exact reconstruction. However, as the sparsity and spatiotemporal correlation deteriorate, there can be crosstalk of signals from different portions of the imaging volume. This crosstalk has generally forced the use of narrow sliding window composites to improve waveform fidelity. Since the sliding window composite has fewer projections, it has more artifact than a full-length composite would. A HYPR-based method presented here uses the concept of local reconstruction (HYPR LR) by constraining the unfiltered backprojected information to local regions in order to reduce the crosstalk and improve waveform fidelity. Simulations were performed to compare the new HYPR LR method to the original HYPR method and determine properties of the new method.

THEORY

In the original HYPR algorithm the unfiltered backprojection process spreads the weighting ratios across the entire image, as shown in Fig. 1a,b. Conceptually, projections

[1]Department of Medical Physics, University of Wisconsin, Madison, Wisconsin.

[2]Department of Physics, University of Wisconsin, Madison, Wisconsin.

[3]Department of Radiology, University of Wisconsin, Madison, Wisconsin.

Part of this article was presented at the 2007 ISMRM Non-Cartesian Workshop.

*Correspondence to: Kevin Johnson, University of Wisconsin – Madison, Department of Radiology, J5/M119 Clinical Science Center, 600 Highland Ave., Madison, WI 53792-3252. E-mail: kmjohnson3@wisc.edu

Received 17 May 2007; revised 12 November 2007; accepted 14 November 2007.

DOI 10.1002/mrm.21505
Published online in Wiley InterScience (www.interscience.wiley.com).

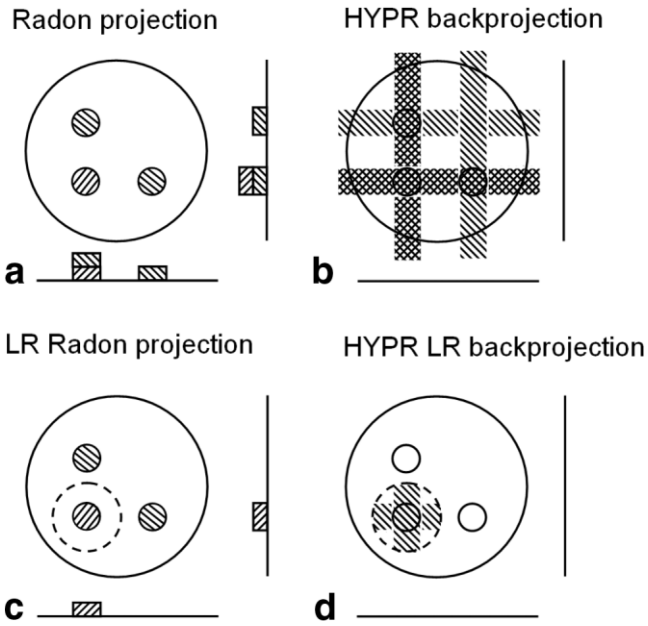

FIG. 1. Schematic comparison of backprojection used in HYPR and HYPR LR. **a:** Radon projection, inherent to the original HYPR, adds mixed temporal information together. **b:** HYPR weighting images are reconstructed used unfiltered backprojection which spreads information across the whole image. **c:** When the Radon projection is done locally by calculating the line integral over a local region, it contains information only about the local region. **d:** A localized unfiltered backprojection, which deposits the local projection information into this local region, effectively avoids the crosstalk between objects.

could be made more local by reconstructing filtered backprojection (FBP) images for each timeframe and then reprojecting parts of the image volume confined to local regions of interest (ROIs) as shown in Fig. 1c. The resulting localized projections only contain the information about a locally defined region. Such projection information is then uniformly backprojected along portions of lines within the local region giving more accurate prediction of the weighting information, as shown in Fig. 1d. Note that we do not necessarily have to reproject localized information along the same projection angles at which the original *k*-space data were acquired. In fact, an arbitrary number of projection angles can be realized. As we increase the number of projection angles and shrink the local ROI the sum of these local projections becomes the sum of the signal values in the region of local reconstruction, and is equivalent to the value obtained by convolving the image with a local uniform filter (a disk function). A series of weighting images can be formed by passing both the individual timeframe and composite images through such a filter and taking their ratio. Finally, these weighting images are multiplied by the composite image to obtain the HYPR LR reconstruction for local ROIs. Mathematically, this procedure can be expressed as follows:

$$I_H(t) = I_C \cdot \frac{F \otimes I_t}{F \otimes I_c^t} \qquad [2]$$

where F is a convolution kernel, I_t is the FBP reconstruction of an individual timeframe, and I_c and I_c^t are the composite images. The additional superscript "t" on the composite images is a reminder that the composite image I_c has been reprojected at the same angles as in the current timeframe image I_t. This reprojection is beneficial in reducing the unwanted streak artifacts, although not necessary if artifacts in the timeframe image have been effectively removed by F.

We can generalize the above image reconstruction formula to suit arbitrary sampling trajectories:

$$I_H(t) = I_c \cdot I_w(t) = I_C \cdot \frac{\Phi(k_t)}{\Phi(k_c^t)} \qquad [3]$$

where Φ is a reconstruction operation of *k*-space data for the timeframe (k_t) and the composite (k_c^t). For each particular sampling trajectory, Φ is designed to reduce aliasing artifacts and/or improve the SNR of the reconstructed images. In the case of radial imaging where *k*-space is oversampled in the central region, Φ is a low-resolution reconstruction as described above.

We refer to the family of reconstruction techniques (Eq. [3]) as HYPR LR. Figure 2 shows a block diagram of one of several possible implementations of HYPR LR. The *k*-space data for a timeframe can be acquired with a highly undersampled interleaved trajectory, e.g., with radial or spiral sampling (Fig. 2a). The composite image *k*-space data (2b) are formed from all or a subset of the congregate acquired data. In (2c) and (2d) these data are transformed to image space, denoted by I_t and I_c, respectively. A unique composite image for the timeframe *t* is constructed as discussed above (2e). These two images are convolved with a kernel chosen to preserve the local temporal behavior in the smallest vessels of interest (2f) and (2g). The weighting image I_w is then obtained (2h) and multiplied by the composite image, I_c, as in the basic HYPR technique (2i) to form the final HYPR LR frame I_H.

It is demonstrated in the Appendix that, as in the original HYPR algorithm, the SNR level of the individual timeframes obtained in the HYPR LR reconstruction is primarily determined by the SNR of the composite image provided that the number of nonzero elements in the convolution kernel *F* is comparable to the number of timeframes in the acquisition.

MATERIALS AND METHODS

The properties of the new HYPR LR method, the original HYPR method, and FBP reconstructions of undersampled timeframes were compared using two numerical phantoms consisting of simulated vessels with different time courses for a contrast-enhanced angiography exam. The first numerical phantom represents an extreme case, where a circular "artery" with 16 pixel diameter is surrounded by a half annulus "vein" with thickness of 16 pixels. The distance between the two vessels is 25 pixels. The second numerical phantom represents another extreme case, where a circular "artery" and a circular "vein," both 16 pixels in diameter, are separated by just two pixels. The image matrix is 256 × 256. All sampling was performed in

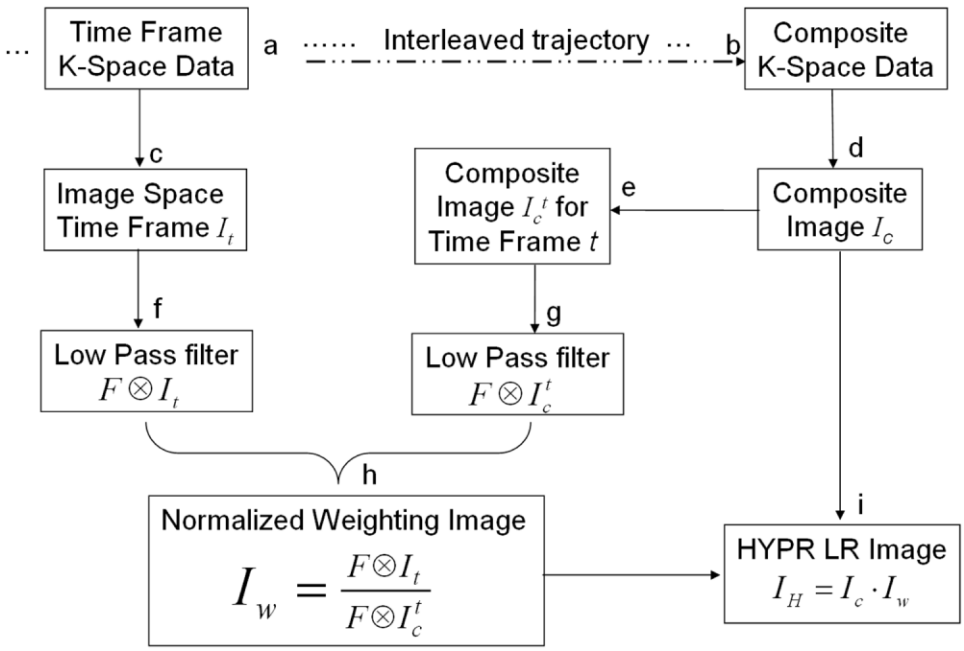

FIG. 2. Schematic of HYPR LR for radial sampling with convolution-based filtering reconstruction.

k-space with independently realized real and imaginary Gaussian noise, 1.5% of the peak image amplitude. To avoid differences due to truncation and sampling error, truth images were created using a noise-free fully sampled acquisition.

Forty sequential images in the time series were formed using 20 interleaved projection angles per image, scheduled using a bit-reversal algorithm. Both HYPR reconstructions were performed using composite images formed from the full time series as well as sliding composite images with windows of 5, 7, and 11 frames centered at each timeframe. Filtering was performed in *k*-space using a radial symmetric Gaussian filter with cutoffs to reduce the resolution by factors of 9, 13, 18, and 27.

The resulting images were evaluated on four criteria: amount and severity of streak artifacts, SNR, waveform, and profile fidelity. For evaluation of both waveforms a 7×7 pixel ROI was placed in both vessels. Noise measurements were done using the same ROI placed on the difference of two independently realized images. Arterial/venous (A/V) ratio curves were calculated by dividing ROI measured arterial curves by the venous curves as a quantitatively measure of arterial-venous separation.

RESULTS

Figure 3 compares the first phantom with the FBP, original HYPR (hyprO), and HYPR LR reconstructions using resolution reduction factors of 9, 18, and 27 (denoted as hyprLR9, hyprLR18, and hyprLR27) for the case of all-inclusive composite images comprising all 40 timeframes. As expected, the streak artifacts are the worst in the FBP reconstruction due to the high level of undersampling. The original HYPR reconstruction has fewer streak artifacts than the HYPR LR9 method, which retains some streaks since it uses weighting images derived from the FBP images. As the weight image resolution is reduced the streaks in the HYPR LR image decrease with minimal distortion of waveforms. Due to the averaging of the composite image over a long period of time, as well as crosstalk between the vessels, the waveforms of the original HYPR reconstruction are not only suppressed in amplitude but also distorted (shifted in space and spread in time). The local nature of HYPR LR is unaffected by the length of the composite image, and waveform fidelity is significantly improved compared to HYPR. There is, however, a dependence on weighting image resolution. When the weighting image resolution is less than the vessel diameter, for case HYPR LR9, the waveforms it generates match the original almost exactly (measured signal deviation less than 1.5%). As the weighting image resolution becomes comparable to the vessel diameter but less than the intervascular distance, as in the case HYPR LR17, averaging with nonvascular signal results in a small (less than 3.9%) suppression of amplitude. The shape of the waveform is maintained. When the weighting image resolution exceeds the distance between two vessels, for case HYPR LR27, averaging with the background and the adjacent vessel not only suppresses the amplitude but also distorts the shape of the waveforms.

Figure 4 shows a similar comparison for the case of sliding composite images with windows of 5 and 11 frames centered at each timeframe. For the original HYPR method, when a narrower 5 frame composite was used (hyprO5), the waveform fidelity improved compared with the wider composite window 11 (hyprO11). This is expected since the composite is now more "local" in time. However, the streak artifacts increased due to the reduced number of projections in the composite images. For the HYPR LR method, changing the duration of the composite image has little effect on the waveforms. However, the use of the longer composite image in the HYPR LR case increases SNR and reduces artifacts of individual timeframes.

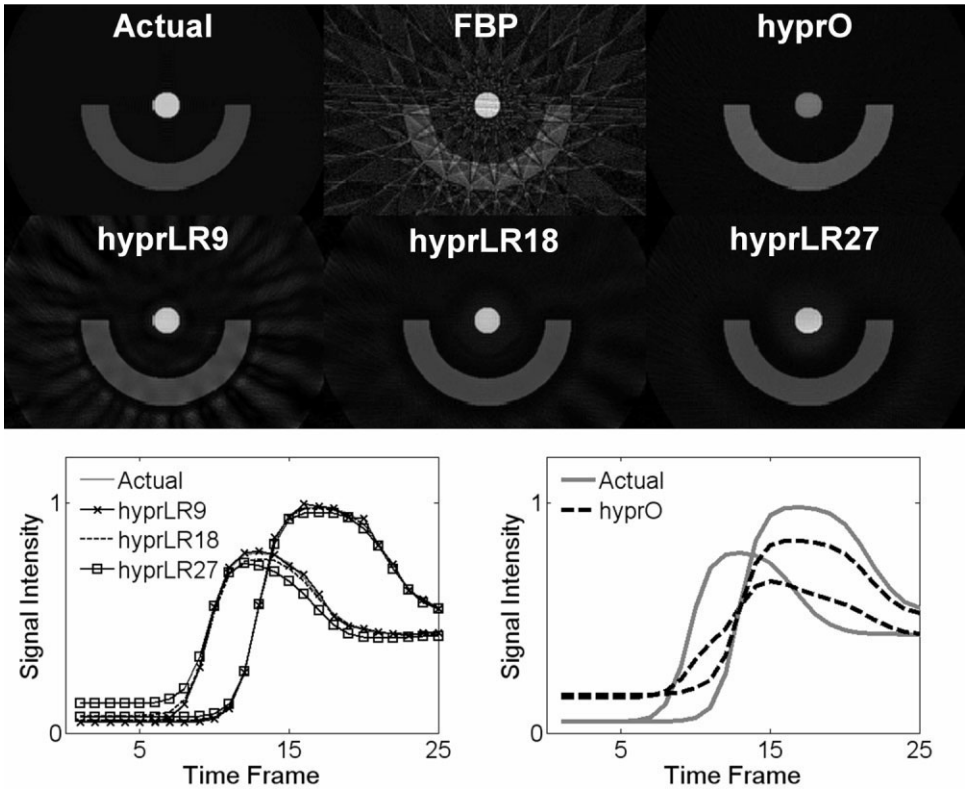

FIG. 3. Comparison of image quality and waveform accuracy using 20 angles per frame and a composite length of 40 frames. Timeframe 12 is shown with the corresponding waveforms of both objects for each method. Original HYPR (hyprO) has the lowest artifact level, but significantly distorts the waveforms. When the weighting image resolution is varied from 1/9th (hyprLR9) to 1/27th (hyprLR27) of the original, artifact levels are reduced at the cost of decreased waveform accuracy.

Figure 5 compares the waveforms and SNR for both methods for a reasonable choice of operating parameters (based on results in Figs. 3 and 4), more precisely, a 7-frame sliding composite image for HYPR reconstruction (hyprO-sw7) and a full composite with a factor of 13 reduction in resolution of the weighting image for the HYPR LR method (hyprLR13). In these examples the waveform fidelity and SNR of the HYPR LR technique are superior to those of the original HYPR.

Figure 6 shows comparison of waveforms for the second phantom, where two circular vessels with different time courses are close to each other. Ten projections per timeframe were used for both HYPR methods. The waveform fidelity and streak content of the HYPR LR technique with factor of 13 reduction in resolution of the weighting image and a full composite image (hyprLR) are improved relative to the original HYPR with a 7-frame composite (hyprO). HYPR LR has better A/V separation than the original HYPR reconstruction and its deviation from the actual A/V ratio of the phantom is less than 5%. Figure 6 also compares the profiles across the two vessels. Since the weighting image resolution for HYPR LR is larger than the intervascular distance, distortion of the vessel profile can be observed. However, the crosstalk is limited only to voxels at the inner edges of the vessels, where the filtering process mixes signals from both vessels. This is not the case for the original HYPR method, where crosstalk is observed across the entire vessels.

DISCUSSION

The results of Figs. 3–6 demonstrate some general trends.

- The HYPR waveform improves as the duration of the composite image is decreased. However, streak artifacts become more pronounced due to the insufficient number of projections in the composite images.
- HYPR LR waveform fidelity has much less dependence on the duration of the composite image than the original HYPR method.
- There is a tradeoff between streak artifacts and waveform fidelity as weighting image resolution of HYPR LR is varied. Lower-resolution weighting images reduce the streak artifacts more. However, when the weighting image resolution is large enough to overlap with two vessels that have different time courses, the shapes of these vascular waveforms may become distorted.
- The HYPR LR waveform fidelity is better than the original HYPR waveform in the case when the waveforms change rapidly or crosstalk of different waveforms becomes problematic.
- The HYPR LR technique has SNR advantages over basic HYPR due to its tolerance of longer composite images.

Although HYPR LR is less influenced by signal crosstalk, waveforms can still be altered when two small vessels with different waveforms are close to each other. For such cases, tradeoffs between waveform fidelity and streak artifacts arise as the weighting image resolution is reduced to preserve the waveform. Simulations shown in this study are based on the 2D case, where streak artifacts are more obvious than 3D case (i.e., VIPR (9)). In the VIPR datasets, undersampling artifacts are spread into 3D, which allows the HYPR LR weighting image resolution to be reduced further to avoid crosstalk from nearby vessels without degrading the image quality.

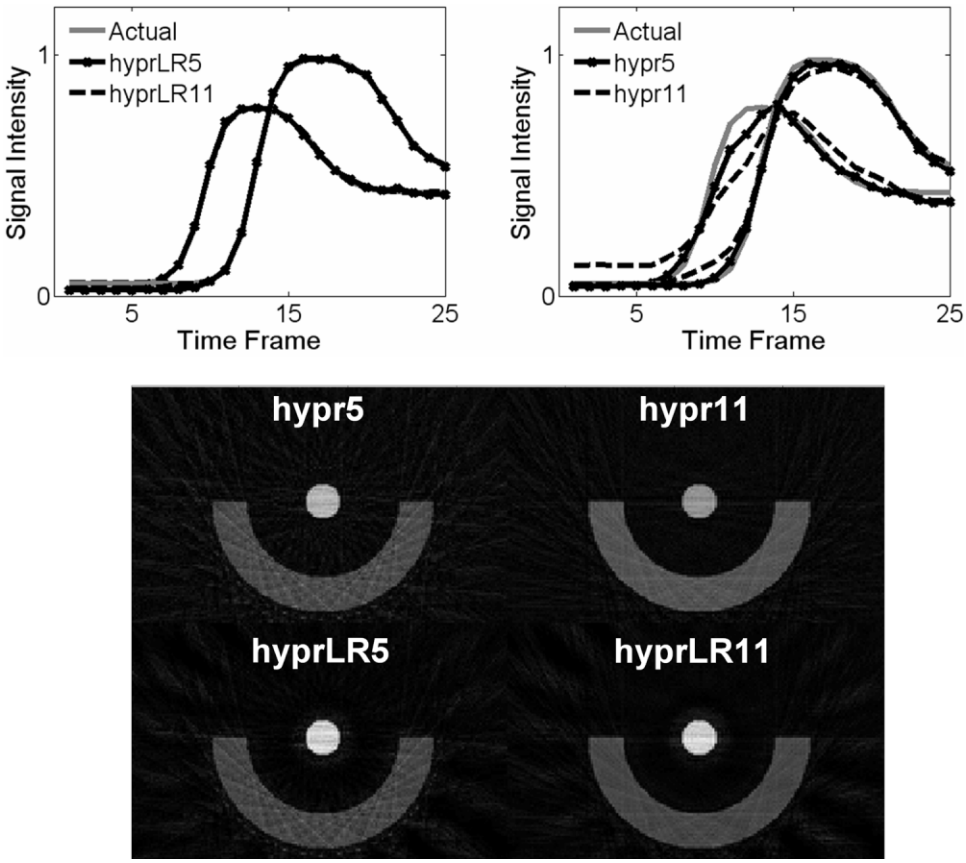

FIG. 4. Comparison of original HYPR and HYPR LR using 20 angles per frame with 5 frame (hypr5,hyprLR5) and 11 frame (hypr5,hyprLR5) sliding window composites. Original HYPR waveforms are improved using a narrow sliding window while HYPR LR images are accurate regardless of the window width. HYPR and HYPR LR images (timeframe 12 shown) are of similar quality, with artifact levels reduced using a wider sliding window.

The simulations performed in this study have several limitations that lead to improved performance of original HYPR processing relative to the realistic situations. While trajectories in the simulations were exact, actual *k*-space trajectories are subject to delays and eddy currents that distort the trajectory. In the original HYPR, these delays cannot be accounted for due to the inherent Radon transform-based reconstruction. On the other hand, since HYPR LR is not restricted to radial acquisitions, trajectory deviations are acceptable and can be accounted for in reconstruction (10). Furthermore, phase effects were ignored in this study. Significant phase variations from phase-array coils and off-resonance can lead to signal cancellation within the acquired projections. While the original HYPR has difficulties in these situations, HYPR LR should perform better, as the weighting images are based on local data which should have more coherent phase. Actual performance with respect to phase variation needs further investigation.

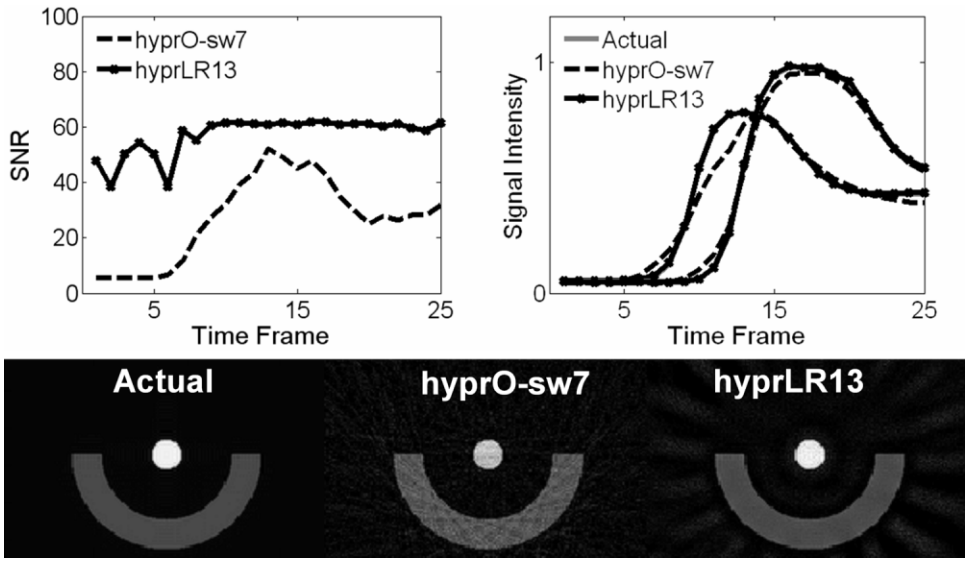

FIG. 5. Comparison of the waveforms, SNR, and image quality for both HYPR methods for a reasonable choice of operating parameters: 20 projections per frame, a 7-frame sliding window composite for original HYPR (hyprO-sw7), and a factor of 13 reduction in weighting image resolution with full composite for HYPR LR (hyprLR13).

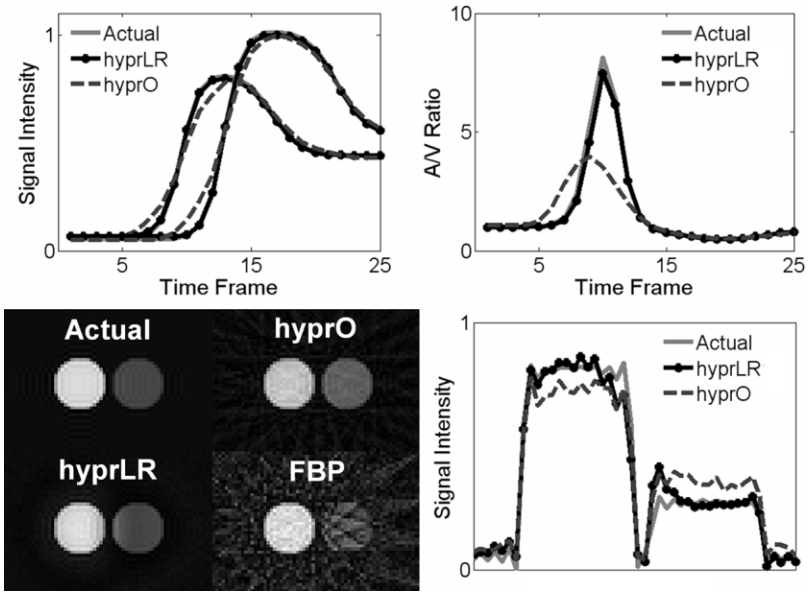

FIG. 6. Comparisons of temporal waveforms, A/V ratios, image quality, and profiles along x for both original HYPR (hyprO) and HYPR LR (hyprLR) with reasonable reconstruction parameters. The ROI averaged signal intensity and A/V ratios of HYPR LR are better correlated with the truth than those of the original HYPR. Images and profiles show the HYPR LR produces distortions at the boundary between the two vessels, while original HYPR shows distortions over a wider area.

In this article we compare HYPR LR only to the original HYPR, although several refinements of the latter have been proposed recently. Iterative HYPR algorithms have been introduced to improve temporal waveform fidelity (11–13). Furthermore, a slightly different HYPR implementation interchanging the order of backprojection and normalization was proposed (14):

$$I_H(t) = I_c \cdot \left(\sum_{i=1}^{N_p} B(P_t^i) \right) \left(\sum_{i=1}^{N_p} B(P_c^i) \right)^{-1}. \quad [4]$$

This formulation leads to a HYPR LR reconstruction with a $1/|k_r|$ convolution filter. In a similar fashion, the HYPR LR operators may be interchanged to yield an alternative HYPR LR reconstruction:

$$I_H(t) = I_C \cdot \left(F \otimes \frac{I_t}{I_c^t} \right) \quad [5]$$

Unlike the original HYPR, where Eqs. [1] and [4] yield similar results, use of Eq. [5] instead of Eq. [2] results in a spatial blurring, as shown in Fig. 7. There is evidence that using a different convolution filter, such as the median filter in Eq. [5], improves the performance of this alternative algorithm. The various iterative and noniterative formulations of HYPR require comparison with respect to composite-length, reconstruction time, spatiotemporal correlation, noise performance, and temporal response. It is likely that for some situations some HYPR reconstructions may be more appropriate than others. For example, in cases of significant motion, spatiotemporal correlation will be very limited, leading to reduced performance of noniterative HYPR methods. In these cases, iterative methods may have improved performance at the cost of increased noise and processing complexity.

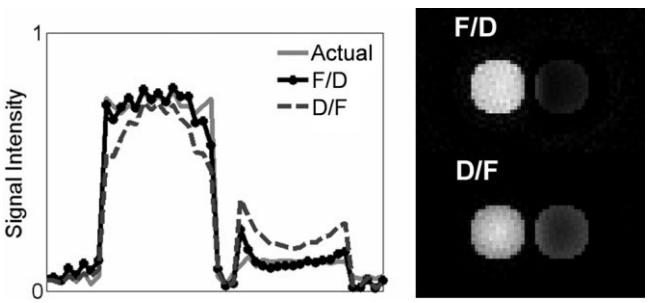

FIG. 7. Effects of changing the order of operations in HYPR LR. Filtering then dividing (F/D, Eq. [2]) results in sharper edges than dividing then filtering (D/F, Eq. [5]) with no significant difference regarding streak artifacts.

CONCLUSIONS

HYPR LR provides potential advantages such as improved waveforms and SNR, but involves tradeoffs in streak artifacts that depend on the size of the weighting image resolution used in the reconstruction. HYPR LR can be easily applied to images generated by arbitrary *k*-space trajectories and reconstruction time is significantly shorter than for iterative methods and the original HYPR algorithm.

APPENDIX (NOISE CONSIDERATIONS)

In order to estimate variance of noise in images reconstructed using HYPR LR algorithm we use the so-called Delta Method (15), stating that if G is a function of random variables (x_i), then $Var(G) \approx \sum_i \sum_j \frac{\partial G}{\partial x_i} \frac{\partial G}{\partial x_j} Cov(x_i, x_j)$. In the case of HYPR LR this amounts to:

$$Var(H) \approx \left(\frac{I_t^k}{I_c^k} \right)^2 Var(C) + \left(\frac{C}{I_c^k} \right)^2 Var(I_t^k) + \left(\frac{C \cdot I_t^k}{I_c^{k2}} \right)^2 Var(I_c^k) + 2 \left(\frac{C \cdot I_t^{k2}}{I_c^{k3}} \right) Cov(C, I_c^k) + 2 \left(\frac{C \cdot I_t^k}{I_c^{k2}} \right) Cov(C, I_t^k) + 2 \left(\frac{C^2 \cdot I_t^k}{I_c^{k3}} \right) Cov(I_t^k, I_c^k) \quad [6]$$

To find values of the individual terms in this formula, we note that the noise in MR images usually comes from the electric noise in the acquired *k*-space samples. The stochastic noise in the reconstructed individual timeframes images can be modeled as additive independently identically distributed Gaussian noise with zero mean and variance $Var(I_t^k) = \sigma^2$. Since the composite image C is averaged over a temporal window of N_f frames, its variance is $Var(C) = \sigma^2/N_f$. When we convolve the composite image with a kernel F (whose elements are normalized so that they sum up to 1), this further decreases the variance of the resulting image, $Var(C) = \sigma^2/(N_f N_K)$, where N_K is the number of nonzero elements in the convolution kernel. The same holds true for the filtered individual timeframe images, $Var(I_t^k) = \sigma^2/N_K$. In order to find covariance between noise in pixel values in the composite and filtered composite images, we use the definition of convolution and properties of covariance to obtain:

$$Cov(C,I_c^k) = Cov(C(x), \sum F(x-y)C(y)) = \sum F(x-y)Cov(C(x),C(y)) = F(0)Var(C(x)), \quad [7]$$

since all summands but one are negligible per our assumption about the nature of stochastic noise. Finally, because the composite image is typically averaged over a long temporal window, the noise in individual timeframes is practically uncorrelated with the noise in the composite image, more so in the filtered composite image I_c^k. Hence, the last two terms in Eq. [6] can be neglected. Therefore, taking into account the fact that all three images C, I_c^k, and I_t^k have the same order of magnitude, we obtain:

$$Var(H) \approx \frac{\sigma^2}{N_f} + \frac{\sigma^2}{N_K} + \frac{\sigma^2}{N_f N_K} + F(0)\frac{\sigma^2}{N_f} = \frac{\sigma^2}{N_f}\left(1 + \frac{N_f}{N_K} + \frac{1}{N_K} + F(0)\right) \quad [8]$$

Since in practice the number of nonzero elements in the convolution kernel is comparable to the number of timeframes (e.g., $N_K = 81$ or 169 and $N_f = 40$ in the simulations in this study) and for the uniform convolution kernel $F(0) = 1/N_K$, we obtain that the SNR in the HYPR LR reconstructed images is primarily determined by the SNR of the composite image used in the reconstruction ($Var(H)$ is on the order of 1.25–1.5 $Var(C)$ in the examples in this article.

REFERENCES

1. Chandra A, Liang ZP, Webb A, Lee H, Morris HD, Lauterbur PC. Application of reduced-encoding imaging with generalied-series reconstruction (RIGR) in dynamic MR imaging. J Magn Reson Imaging 1996; 6:783–797.
2. Tsao J, Boesiger P, Pruessmann KP. k-t BLAST and k-t SENSE: dynamic MRI with high frame rate exploiting spatiotemporal correlations. Magn Reson Med 2003;50:1031–1042.
3. Mistretta CA, Wieben O, Velikina J, Block W, Perry J, Wu Y, Johnson K, Wu Y. Highly constrained backprojection for time-resolved MRI. Magn Reson Med 2006;55:30–40.
4. Candes EJ, Romberg J. Robust uncertainty principles: exact signal reconstruction from highly incomplete frequency information. IEEE Inf Theory 2006;52:489–509.
5. Lustig M, Santos JM, Donoho DL, Pauly JM. k-t SPARSE: high frame rate dynamic MRI exploiting spatio-temporal sparsity. In: Proc 14th Annual Meeting ISMRM, Seattle, WA; 2006:2420.
6. Wieben O, Velikina J, Block WF, Perry J, Wu Y, Johnson KM, Wu Y, Korosec FR, Mistretta CA. Highly constrained back projection (HYPR): theory and potential applications. In: Proc 14th Annual Meeting ISMRM; Seattle, WA; 2006:688.
7. Velikina J, Mistretta CA, Johnson KM, Wieben O. An application of highly constrained backprojection (HYPR) to time-resolved VIPR acquisition. In: Proc 13th Annual Meeting ISMRM, Seattle, WA; 2006: 692.
8. Wu YJ, Wu Y, Korosec FR, Wieben O, Du J, Mistretta CA. HYPR PR-TRICKS: highly undersampled hybrid radial/Cartesian acquisition with highly constrained backprojection reconstruction for time resolved MRI. In: Proc 14th Annual Meeting ISMRM, Seattle, WA; 2006: 335.
9. Barger AV, Block WF, Toropov Y, Grist TM, Mistretta CA. Time-resolved contrast-enhanced imaging with isotropic resolution and broad coverage using an undersampled 3D projection trajectory. Magn Reson Med 2002;48:297-305.
10. Duyn JH, Yang YH, Frank JA, van der Veen JW. Simple correction method for k-space trajectory deviations in MRI. J Magn Reson 1998; 132:150–153.
11. Griswold M, Barkauskas K, Blaimer M, Moriguchi H, Sunshine J, Duerk JL. More optimal HYPR reconstructions using a combination of HYPR and conjugate–gradient minimization. Proceedings of MRA Club, Basel, Switzerland; 2006:29.
12. O'Halloran RL, Holmes J, Fain SB. Iterative reconstruction of time-resolved projection images using highly constrained back projection (HYPR). In: Proc ISMRM Non-Cartesian Workshop, Sedona, AZ; 2007.
13. Samsonov AA, Wieben O, Block WF. HYPRIT: generalized HYPR reconstruction by iterative estimation. In: Proc ISMRM Non-Cartesian Workshop, Sedona, AZ; 2007.
14. Yuexi Huang GAW. Time-resolved MR angiography with limited projections. Magn Reson Med 2007;58:316-325.
15. Klein LR. A textbook of econometrics. Evanston, IL: Row, Peterson; 1953.